

A 65 nm Bayesian Neural Network Accelerator with 360 fJ/Sample In-Word GRNG for AI Uncertainty Estimation

Zephan M. Enciso¹, Boyang Cheng², Likai Pei², Jianbo Liu², Steven Davis², Ningyuan Cao², and Michael Niemier¹

¹Department of Computer Science and Engineering, University of Notre Dame

²Department of Electrical Engineering, University of Notre Dame

Abstract—Uncertainty estimation is an indispensable capability for AI-enabled, safety-critical applications, e.g. autonomous vehicles or medical diagnosis. Bayesian neural networks (BNNs) use Bayesian statistics to provide both classification predictions and uncertainty estimation, but they suffer from high computational overhead associated with random number generation and repeated sample iterations. Furthermore, BNNs are not immediately amenable to acceleration through compute-in-memory architectures due to the frequent memory writes necessary after each RNG operation. To address these challenges, we present an ASIC that integrates 360 fJ/Sample Gaussian RNG directly into the SRAM memory words. This integration reduces RNG overhead and enables fully-parallel compute-in-memory operations for BNNs. The prototype chip achieves 5.12 GSa/s RNG throughput and 102 GOP/s neural network throughput while occupying 0.45 mm², bringing AI uncertainty estimation to edge computation.

I. INTRODUCTION

Uncertainty estimation is crucial for robust decision-making in data-driven deep learning (DL) systems, particularly when these systems interact with the physical environment. In safety-critical applications, such as autonomous vehicle navigation and obstacle avoidance, medical diagnosis, aerospace control systems, and industrial automation, models equipped with uncertainty estimation could trigger human intervention or engage alternative sensors and models when prediction confidence drops below a set threshold. This process significantly mitigates the risk of potential catastrophic outcomes (see Fig. 1).

Bayesian neural networks (BNNs) provide a DL framework capable of delivering probabilistic estimates of classification uncertainty by replacing conventional deterministic weights with a posterior distribution of weights [1], [2]. Deployed models typically approximate the posterior with Gaussian distributions [3], [4]; even so, BNNs incur significant overheads from Gaussian random number generation (GRNG), the associated memory accesses, and repeated inferences, as shown in Fig. 2.

Moreover, BNNs derive less benefit from non-Von Neuman architectures, such as compute-in-memory (CIM) [5], [6]. When BNNs are deployed on these architectures, the GRNG must retrieve distribution parameters from memory, generate a weight sample, and subsequently write the sample back to

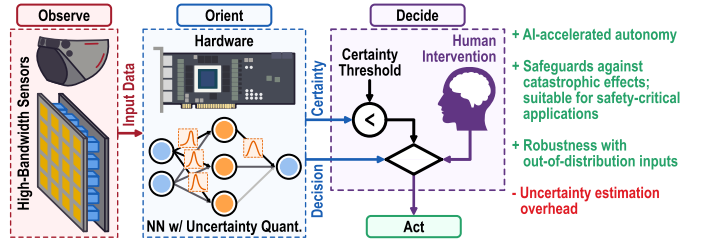


Fig. 1. The role of uncertainty estimation in safety-critical applications. During typical operation, the model rapidly performs autonomous actions. However, if the model’s certainty falls below a predetermined threshold, it would request human intervention to avoid catastrophic effects.

the CIM array. Simulations indicate that even CIM-accelerated BNNs consume more than six times the energy per INT8 operation in each sampling iteration compared to traditional neural networks [7], [8] (see Fig. 2), increasing the cost of deploying them on edge inference engines.

Current BNN accelerators focus primarily on either enhancing the efficiency of GRNG hardware [9]–[15] or maximizing data reuse [16]. By contrast, this chip performs fully parallel, in-memory matrix-vector multiplication with arbitrary Gaussian weight distributions. Crucially, this is achieved without requiring extra memory accesses for the GRNG, as the GRNG is integrated within the memory words. This stochastic, mixed-signal CIM architecture, combined with state-of-the-art (SOTA) GRNG energy and area efficiency, enables energy- and area-efficient BNN acceleration.

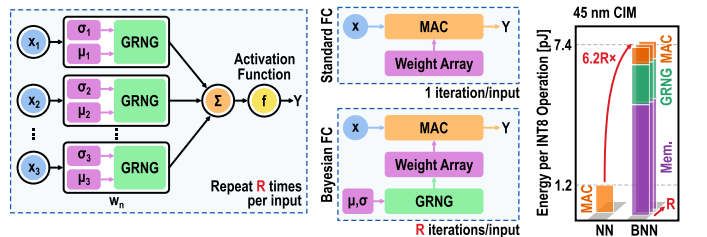


Fig. 2. **Left**) Conventional BNN neuron. Each weight uses GRNG to sample from a Gaussian distribution, so the weight must store distribution properties μ and σ . **Right**) BNN fully-connected (FC) layers incur significant overhead from multiple memory operations and GRNG compared to standard FC layers.

II. BACKGROUND

A. Bayesian Neural Networks

Bayesian neural networks (BNNs) augment traditional neural networks by encoding weights and biases as posterior distributions, which facilitates a probabilistic interpretation of model predictions [17]. This probabilistic approach enables BNNs to provide both classification predictions and uncertainty estimations.

Formally, the posterior distribution of weights follows Bayes' Theorem:

$$P(\mathbf{W} | \mathbf{X}, \mathbf{Y}) = \frac{P(\mathbf{Y} | \mathbf{W}, \mathbf{X}) P(\mathbf{W})}{P(\mathbf{X})} \quad (1)$$

where:

- $P(\mathbf{W} | \mathbf{X}, \mathbf{Y})$ denotes the posterior probability of weights \mathbf{W} given input \mathbf{X} and output \mathbf{Y} .
- $P(\mathbf{Y} | \mathbf{W}, \mathbf{X})$ is the conditional probability or likelihood of observing outputs \mathbf{Y} for weights \mathbf{W} and input \mathbf{X} .
- $P(\mathbf{W})$ and $P(\mathbf{X})$ are the prior probabilities of the weights and input, respectively.

Directly approximating the posterior distribution $P(\mathbf{W} | \mathbf{X}, \mathbf{Y})$ is computationally intractable for edge devices. Consequently, deployed models typically approximate the posterior with a Gaussian distribution through a method known as variational inference (VI) [4]. This approximation is expressed as:

$$P(\mathbf{W} | \mathbf{X}, \mathbf{Y}) \approx \mathcal{N}(\mathbf{W} | \mu, \sigma) \quad (2)$$

where:

- μ is the mean of the Gaussian distribution.
- σ is the covariance matrix of the Gaussian distribution.

The process of approximating the posterior distribution involves minimizing the divergence between the true posterior and the approximated Gaussian distribution. This minimization is commonly achieved by maximizing the evidence lower bound (ELBO), a technique that balances the fit of the model to the data with the complexity of the model [3].

B. Compute-in-Memory Accelerators

Compute-in-memory (CIM) is an emerging accelerator architecture designed to address the von Neumann bottleneck, which refers to the significant latency and power consumption resulting from the separation of memory and processing units in traditional computing architectures. By integrating memory and computation, CIM accelerators aim to reduce data movement, thereby improving both energy efficiency and performance [7], [18]. This integration is particularly beneficial for DL applications, where the energy cost and latency of frequent memory access can be substantial and memory access patterns are relatively simple.

One of the key principles behind CIM is the use of crossbar arrays for performing matrix-vector multiplications (MVMs) directly within the memory [19]. In a crossbar array, the matrix weights are encoded as the conductance $\mathbf{G}_{(i,j)}$ of each memory cell. When a voltage \mathbf{X}_i is applied to each row, it

induces a current \mathbf{Y}_j to flow down each column according to Kirchhoff's Law. Mathematically, this can be represented as:

$$\mathbf{Y}_j = \sum_i^N \mathbf{X}_i \mathbf{G}_{(i,j)} \quad (3)$$

Thus, $\mathbf{Y} = \mathbf{G} \cdot \mathbf{X}$, and this direct in-memory computation reduces the need for data transfer between memory and computation units.

Crossbars also support parallel in-memory operations. Depending on the precision and number of downstream analog-to-digital converters (ADCs), multiple rows and columns may be activated concurrently. This parallelism enables CIM accelerators to perform high-throughput computation, which is essential for DL applications that require extensive MVMs. CIM designs have been realized with both static random-access memory (SRAM) and emerging memory technologies (EMTs), such as resistive random-access memory (ReRAM), phase-change memory (PCM), and spin-transfer torque magnetic random-access memory (STT-MRAM) [20]–[22]. These technologies may offer advantages in terms of storage density and non-volatility, making them suitable for different application requirements.

C. BNN Hardware Acceleration

BNNs are distinguished from conventional neural networks by their reliance on stochastic sampling, which significantly amplifies hardware resource demands. This stochastic process necessitates extensive inference runs to accurately determine the mean and variance of inference scores, thereby assessing model uncertainty. Digital BNN accelerators focus on optimizing GRNG [14], [15] or improving the hardware architecture pipeline through data reuse strategies that minimize unnecessary data transactions [12], [16]. Despite these efforts, an efficiency gap remains due to the limitations of digital GRNG and the frequency of memory operations required for BNN inference.

Each inference iteration in a BNN involves reading distribution parameters, generating a Gaussian sample, and subsequently updating the weight array. This iterative process makes it challenging to apply CIM architectures for BNN hardware acceleration. Leveraging the stochastic properties of EMTs, can enable efficient GRNG through device variation [23]. These emerging memory technologies exploit the inherent stochasticity in their physical properties to generate noise with the stored data, thereby integrating GRNG with memory.

However, the dependency on specific device characteristics for generating stochasticity, coupled with the high power consumption of memory writes for storing GRNG results, introduces programming complexities and scalability issues. Additionally, the endurance and durability concerns of these technologies further complicate their long-term viability for BNN acceleration.

III. CHIP ARCHITECTURE AND CIRCUIT DESIGN

A. Hardware-Software Co-Design

This chip employs several algorithmic optimizations to reduce BNN overhead and simplify GRNG. First, SOTA

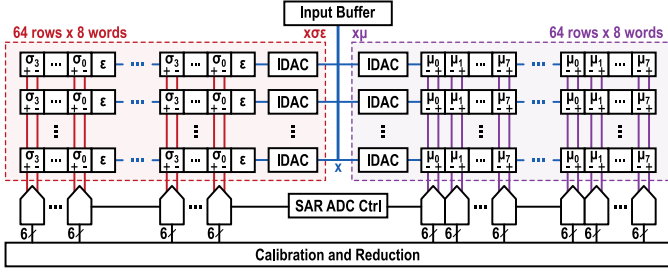


Fig. 3. CIM tile architecture, featuring two subarrays for separately computing $X\sigma\epsilon$ and $X\mu$. Both subarrays receive the same input X , and downstream reduction logic recombines the results.

Bayesian accelerators typically employ Bayesian weights only to the last fully-connected (FC) layers (“partial BNN”). These layers are critical for generating a classification from previously-extracted features and thus have the largest impact on uncertainty. By doing so, partial BNNs significantly reduce the number of repeated operations and the requisite number of RNG samples. Meanwhile, the computationally-expensive convolutional and/or recurrent layers are processed as standard, non-Bayesian layers. This strategy maintains the model’s ability to quantify uncertainty without incurring excessive computational costs [13].

A key optimization in this architecture is weight decomposition, which separates each weight into a sum of the mean μ and the product of its standard deviation σ and a distribution sample ϵ :

$$w_{(i,j)} = \mu_{(i,j)} + \sigma_{(i,j)}\epsilon, \quad \epsilon \sim \mathcal{N}(0, 1) \quad (4)$$

Thus, the j^{th} output Y_j with N inputs $X_{(i,j)}$ is given by:

$$Y_j = f \left(\sum_{i=1}^N X_{(i,j)}\mu_{(i,j)} + \sum_{i=1}^N X_{(i,j)}\sigma_{(i,j)}\epsilon \right) \quad (5)$$

Since the mean μ is static, it only needs to be processed once. Furthermore, ϵ is sampled from the same standard normal distribution instead of a parameterized normal distribution, which significantly simplifies the GRNG design. This simplification is crucial because it reduces the computational burden associated with generating and storing multiple unique random samples for each weight update.

B. CIM Tile Architecture

The CIM tile architecture is designed to reflect the weight decomposition methodology, as shown in Fig. 3, by using two crossbar subarrays for separately computing $X\mu$ and $X\sigma\epsilon$. In the fabricated prototype, each CIM tile comprises 64 rows of 8 words. Each word consists of a 8-bit μ and a 4-bit σ . The 4-bit digital input vector X is fed to current digital-to-analog converters (IDACs). Each word bit is associated with a dedicated 6-bit successive-approximation register (SAR) ADC.

To enhance efficiency, the SAR ADCs share a common synchronous controller. This shared control reduces the overall area requirement for each ADC and enables pitch-matching

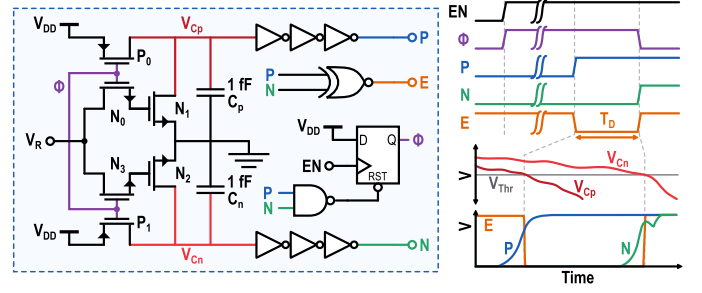


Fig. 4. GRNG circuit and timing diagram. Thermal noise causes C_n to discharge at a different rate than C_p , producing an output pulse E whose duration follows a 0-mean Gaussian distribution.

with the SRAM arrays. Pitch-matching is critical as it eliminates the need for column multiplexing, thus enabling single-cycle MVM.

The CIM tile also includes digital reduction logic, which also corrects for individual ADC offset. This logic shifts and adds the outputs from the SAR ADCs to reconstruct each word. Once the individual components of $X\mu$ and $X\sigma\epsilon$ have been computed, they are combined to generate a single output vector.

C. In-Word GRNG Circuit

1) *Capacitor Thermal Noise*: Unlike pseudorandom RNGs, true RNGs (TRNG) require a physical process capable of producing entropy [24]. Common entropy sources for integrated circuits include thermal noise, jitter, and electrical metastability [25]. [26] identified that thermal noise affects the discharge period of a capacitor with constant leakage current, and the discharge follows a Gaussian distribution whose properties are given by:

$$\mu_T = \frac{CV_{DD}}{2I_L} \quad (6)$$

$$\sigma_T^2 = \frac{\mu_T q}{2I_L} \quad (7)$$

where:

- μ_T is the mean or expectation of the distribution.
- σ^2 is the variance of the distribution.
- C is the capacitance of the capacitor being discharged.
- I_L is the total leakage current.
- q is the initial charge on the capacitor.
- T represents the time after the capacitor begins leaking that the voltage crosses threshold V_{Thr} .

2) *GRNG Operation*: The in-word GRNG circuit (see Fig. 4) that enables CIM-accelerated BNNs compares the discharge time of two capacitors C_p and C_n to yield a normal distribution centered on zero. The process involves the following steps:

- 1) Initially P_0 and P_1 charge C_p and C_n to V_{DD} while Φ is low.
- 2) Pulling EN high latches Φ and causes N_1 and N_2 —biased to V_R through N_0 and N_3 , respectively—to slowly discharge C_p and C_n to ground.

- 3) The inverters at nodes V_{Cp} and V_{Cn} sharpen the transition over inverter threshold V_{Thr} , yielding digital signals P and N, which represent a positive and negative value, respectively.
- 4) The output E is the logical XNOR of P and N, and E represents the sampled random variable encoded in the time domain. T_D , the width of output pulse E, follows a Gaussian distribution; Sec. IV-A validates the normality of the output distribution with measured results.

The capacitors C_p and C_n are designed to be small (~ 1 fF) to minimize discharge energy. They are physically implemented as metal fringe capacitors directly above the GRNG circuit for optimal area utilization and mismatch performance [27]. The inverters dissipate the majority of the GRNG power because they create a weak conduction path from V_{DD} to ground as V_{Cp} and V_{Cn} approach V_{Thr} . To mitigate inverter power consumption, the GRNG circuit also includes an asynchronous reset D flip-flop (DFF), which resets Φ when E goes high, charging V_{Cp} and V_{Cn} back to V_{DD} and eliminating the conduction path.

3) *Calibration for Static Variation:* Transistor mismatch induced during fabrication may cause either N_1 or N_2 to conduct current faster than the other for the same applied gate voltage. This static variation manifests as a non-zero mean ϵ_0 in the output distribution:

$$\epsilon_0 = V_{DD} \left(\frac{C_p I_{N2} - C_n I_{N1}}{2 I_{N1} I_{N2}} \right) \neq 0 \quad (8)$$

Subthreshold operation, which is required to produce adequately large standard deviations, further amplifies the effects of transistor variations [28]. However, such deviation is static—for a given die, the same variation will be observed each cycle—and can be systematically corrected through calibration. First, the chip measures the mean offset $\epsilon_{0,(i,j)}$ for weight $w_{(i,j)}$ by writing 1 to all σ words and multiplying each row by 1 sequentially. Then, the static offset is subtracted from the μ cell, resulting in calibrated weight $w'_{(i,j)}$:

$$w_{(i,j)} = \mu_{(i,j)} + \sigma_{(i,j)} (\epsilon + \epsilon_{0,(i,j)}) \quad (9)$$

$$w'_{(i,j)} = \mu'_{(i,j)} + \sigma_{(i,j)} \epsilon, \quad \mu'_{(i,j)} = \mu_{(i,j)} - \sigma_{(i,j)} \epsilon_0 \quad (10)$$

The entire calibration process consumes 3.6 nJ and must only be performed once per chip, though subsequent weight changes must be updated to include the offset.

D. CIM Memory Words

The CIM memory words, as depicted in Fig. 5, use 8T SRAM cells to minimize parasitic leakage current. These cells feature separate wordlines (WLs) and bitlines (BLs) for reading and writing operations. The computation process begins by charging all BLs to V_{DD} . Subsequently, each row's IDAC converts the 4-bit digital input \mathbf{X}_i into a read WL voltage. This voltage ensures that the current conducted by the 8T SRAM cells is linearly proportional to \mathbf{X}_i . The cells conduct current from the BLs to ground for a set duration, and the resulting voltage on the j^{th} BL represents the vector dot product of \mathbf{X} by all cells connected to BL_j .

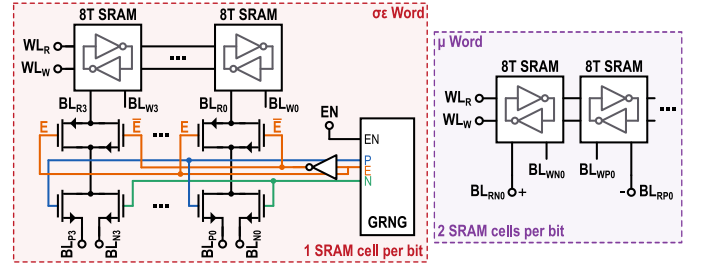


Fig. 5. $\sigma\epsilon$ and μ CIM word circuits. The $\sigma\epsilon$ word contains additional switches to interface with the GRNG and produce a differential output. The μ word's output is differential because the data is stored differentially across 2 SRAM cells per bit.

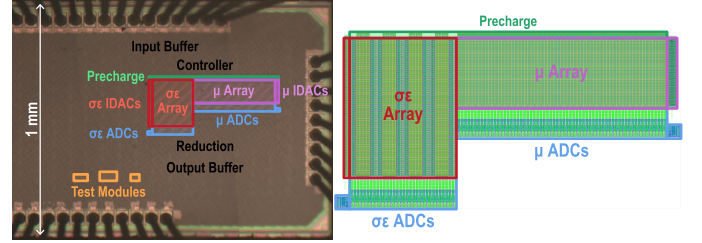


Fig. 6. **Left:** Annotated die shot showing CIM tile (colored outlines) and supporting digital logic (black). The number of IO pads were limited to decrease package size and thus decrease bond wire capacitive coupling. **Right:** Detailed view of the CIM tile.

To facilitate robust CIM operation, the downstream SAR ADCs operate differentially, with charge on BL_N and BL_P representing negative and positive values, respectively. For differential data encoding in the μ word, each bit uses 2 SRAM cells. A positive value is represented by 01 and a negative value represented with 10. By contrast, the $\sigma\epsilon$ word only requires one SRAM cell per bit because the GRNG produces signed outputs. First, the current through the SRAM cell is gated by GRNG output pulse E via transmission gates at the output. Then, current flows either from BL_P or BL_N depending on complimentary GRNG signals P and N.

IV. HARDWARE EVALUATION

A prototype chip fabricated on a commercial 65 nm PDK (Fig. 6) provides validation measurements for this design. GRNG tests were conducted in a thermal chamber, as shown in Fig. 7 to ensure a stable operating environment and to measure the temperature stability of the GRNG circuit.

A. In-Word GRNG

The output distribution and associated latency for one bias configuration are shown in Fig. 8. An examination of the normal probability plot—a specific type of Q-Q plot used to assess normal distributions—indicates that the output distribution is suitably normal for quantized applications with an r -value of 0.9967 for $N = 2500$ samples.

Since the bias voltage V_R controls the rate at which capacitors N_1 and N_2 discharge C_p and C_n , increasing V_R reduces total energy and GRNG latency but also decreases the output standard deviation. Fig. 9 illustrates the trade-off between average latency and the standard deviation of

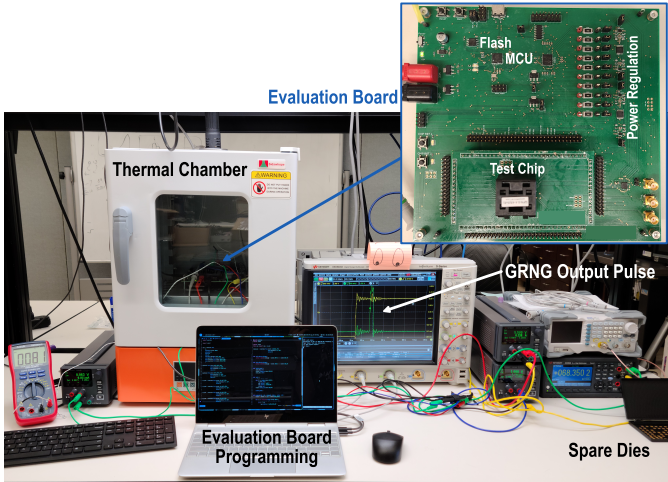


Fig. 7. Measurement setup for obtaining GRNG output distributions. The custom evaluation board rests in a temperature-controlled chamber, and a DSOS404A oscilloscope records output pulses via a N2795A active probe.

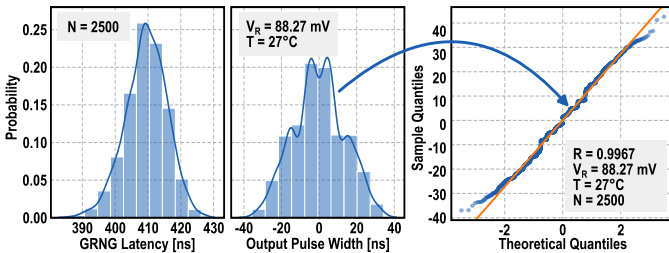


Fig. 8. Sample GRNG output pulse width and latency distributions for one bias and temperature configuration. Normal probability plot (Q-Q plot) examines normality of pulse width distribution; the orange line represents an ideal Gaussian distribution, and the r -value reports how well the line fits the measured data. Output pulses less than 1 ns cannot be reliably measured due to IO constraints.

the output pulse width. Typical operation uses a 180 mV bias voltage to generate an output distribution with a 1.0 ns standard deviation at an average latency of 69 ns, consuming 360 fJ/Sample. However, increasing the bias voltage beyond 110 mV creates an increased proportion of sub-1 ns pulses, which compromises measurement accuracy due to the IO limits of the experimental setup. Therefore, Fig. 9 includes both chip measurements and parasitic-annotated simulation results to provide a comprehensive view of GRNG operating points.

Thermal noise is also sensitive to change in environmental temperature; as the environmental temperature increases from 28 °C to 60 °C, the pulse width standard deviation increases by 2.62 \times , and the average latency decreases by 2.49 \times (see Tab. I). Despite these variations, the quality of the output distribution slightly improves—the normal probability plot r -value increases by 4.78% over the same temperature increase. Furthermore, changes in standard deviation can be compensated for by tuning the IDAC bias, which affects the rate at which the CIM cells conduct current from the bitlines.

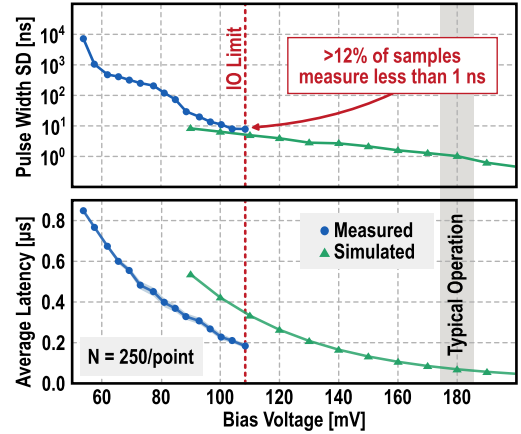


Fig. 9. GRNG operation under different bias configurations. Increasing the bias voltage V_R decreases average latency, but it also reduces the output standard deviation. Off-chip measurements of the GRNG output are constrained by chip IO, so plots also include simulated datapoints.

TABLE I
MEASURED GRNG TEMPERATURE STABILITY

Temperature [°C]	Q-Q r -value	T_D SD [ns]	Avg. Latency [μ s]
28	0.9292	197.1	1.931
40	0.9916	201.9	1.297
50	0.9928	242.2	1.051
60	0.0736	515.5	0.7749

B. Model Uncertainty Estimation

The INRIA person dataset [29] models a safety-critical application where the neural network must accurately identify the presence of pedestrians. MobileNet [30] was chosen for this analysis due to its efficient feature extraction capabilities, which lends itself to edge inference.

Fig. 10 illustrates how BNNs achieve uncertainty estimation by increasing the entropy of incorrect and out-of-distribution classifications. In the standard MobileNet implementation, incorrect classifications typically exhibit low entropy, making them indistinguishable *a priori* from correct classifications. However, when employing a Bayesian classifier (Bayesian FC

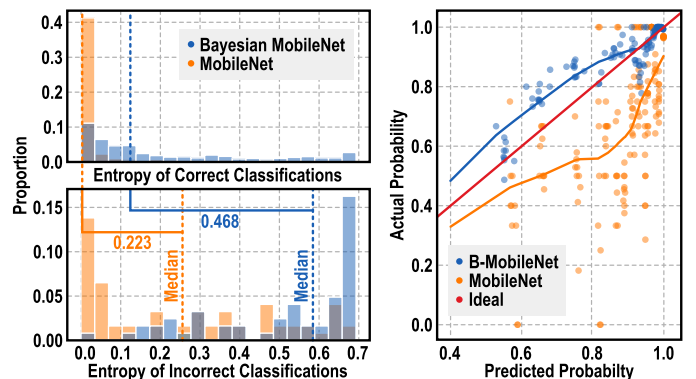


Fig. 10. **Left**) BNNs significantly increase the entropy of incorrect and out-of-distribution classifications, providing more accurate uncertainty estimation. **Right**) Calibration curve showing low BNN ECE compared to the overconfident NN.

TABLE II
COMPARISON TO OTHER WORK

	This Work	[9]	[10]	[11]	[12]	[13]
Implementation	ASIC	ASIC	Simulated	FPGA	FPGA	FPGA
Technology [nm]	65	22	45 (PTM)	28 (Cyclone V)	16 (ZU9EG)	20 (Arria 10)
RNG	Analog (Thermal)	TI-Hadamard	Analog (V_{th} Variation)	Wallace	Box-Muller	MC Dropout
Precision	INT8/4 (Heterogeneous)	INT8/16/32 FP8/16/32 BF16	INT4	INT8	INT16	INT8
Area* [mm²]	0.45	3.88	—	80/17/100/39	2.9/1.4/6.6/8.6	71/52/97/86
Norm. RNG Tput [GSa/s/mm²]	11.4 (62.3)[†]	1.20–1.88	—	—	—	—
RNG Tput [GSa/s]	5.12 (28.0) [†]	4.65–7.31	—	13.63	8.88	—
RNG Eff. [pJ/Sa]	0.36	1.08–1.69	0.37	38.8	5.40	—
Norm. NN Tput [GOp/s/mm²]	228 (1246) [†]	309–515	—	—	—	—
NN Tput [GOp/s]	102	1200–2000	—	59.6	—	533–1590
NN Eff. [fJ/Op]	672	31–65	—	—	—	24000–51000

*Percent utilization of LUT/Register/DSP/BRAM for FPGAs

[†]Scaled to 22 nm

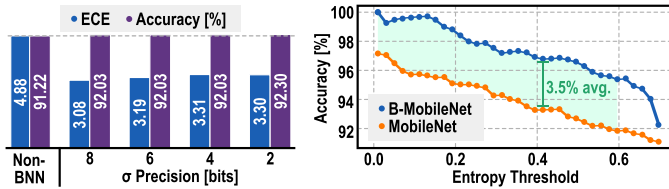


Fig. 11. **Left**) Quantized partial-Bayesian MobileNet ECE and accuracy for the INRIA person dataset compared to a traditional network. **Right**) BNN vs NN accuracy recovery when removing high-entropy classifications. A lower threshold indicates more samples are removed.

layers, see Sec. III-A) on this chip, the the average predictive entropy (APE) of incorrect classifications increases from 0.350 to 0.513 (+46.6%). Concurrently, the expected calibration error (ECE) [31] decreases from 4.88 to 3.31 (-32.2%). ECE measures the total area between the ideal calibration curve (which is linear) and the model’s calibration curve; models with high ECE perform poorly at uncertainty estimation, as demonstrated by the standard MobileNet in Fig. 10.

Even with only 2 bits of σ precision, the partial-Bayesian MobileNet maintains a low ECE (see Fig. 11). However, this chip employs a 4-bit σ to support more complex applications where the model requires more precision to quantify uncertainty accurately.

In a real-world BNN model deployment, classifications with uncertainty exceeding predetermined threshold would be flagged for further scrutiny, either via human intervention or supplemental sensors and models. As demonstrated in Fig. 11, when deferring high-entropy classifications, the partial-Bayesian network outperforms the standard model, achieving an average accuracy recovery of 3.5% for representative entropy thresholds between 0.0 and 0.6. Users can also trade-off overall accuracy for better uncertainty estimation through adjustments to the loss function during training, although such techniques are beyond the scope of this work.

Overall, BNN models deployed on this chip effectively

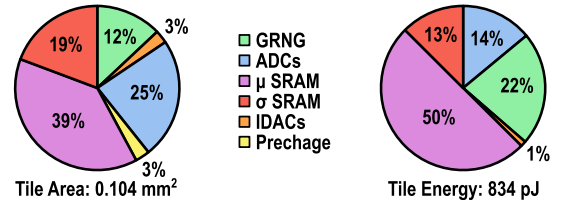


Fig. 12. Tile area and energy breakdown for one complete MVM. Synthesized digital components, such as the calibration and reduction logic and IO buffers, are not included.

retain their uncertainty estimation, confirming this chip’s suitability for safety-critical edge deployments, such as person detection for autonomous vehicles.

V. CONCLUSION

Fig. 12 presents a detailed breakdown of the tile area and energy consumption for one complete MVM. The SRAM accounts for over 63% of the total tile energy and 48% of total tile area, underscoring the power and space efficiency of the in-word GRNG cell. When compared to SOTA BNN ASICs, as detailed in Tab. II, this chip achieves a 75% GRNG energy reduction and increases GRNG throughput by over 6× per mm² at the current tech node or over 33× per mm² when scaled to the same technology.

In conclusion, the integration of a 360 fJ/Sample GRNG directly into SRAM memory words presents a significant advancement in the acceleration of BNNs. By reducing the computational overhead associated with RNG and facilitating fully-parallel CIM operations, this ASIC overcomes the traditional challenges faced by BNN accelerators. The prototype chip validates the potential of this approach to bring efficient AI uncertainty estimation to edge computation without sacrificing model accuracy. This work paves the way for more reliable and robust AI systems in safety-critical environments, ultimately contributing to the broader adoption and implementation of BNNs in high-stakes applications.

REFERENCES

- [1] K. Shridhar, F. Laumann, and M. Liwicki, "A comprehensive guide to bayesian convolutional neural network with variational inference," 2019. [Online]. Available: <https://arxiv.org/abs/1901.02731>
- [2] J. Gawlikowski, C. R. N. Tassi, M. Ali, J. Lee, M. Humt, J. Feng, A. Kruspe, R. Triebel, P. Jung, R. Roscher *et al.*, "A survey of uncertainty in deep neural networks," *Artificial Intelligence Review*, vol. 56, no. Suppl 1, pp. 1513–1589, 2023.
- [3] D. M. Blei, A. Kucukelbir, and J. D. McAuliffe, "Variational inference: A review for statisticians," *Journal of the American statistical Association*, vol. 112, no. 518, pp. 859–877, 2017.
- [4] M. D. Hoffman, D. M. Blei, C. Wang, and J. Paisley, "Stochastic variational inference," *Journal of Machine Learning Research*, 2013.
- [5] R. Khaddam-Aljameh, M. Stanisavljevic, J. F. Mas, G. Karunaratne, M. Brändli, F. Liu, A. Singh, S. M. Müller, U. Egger, A. Petropoulos *et al.*, "Hermes-core—a 1.59-tops/mm² pcm on 14-nm cmos in-memory compute core using 300-ps/lb linearized cco-based adcs," *IEEE Journal of Solid-State Circuits*, vol. 57, no. 4, pp. 1027–1038, 2022.
- [6] P.-C. Wu, J.-W. Su, Y.-L. Chung, L.-Y. Hong, J.-S. Ren, F.-C. Chang, Y. Wu, H.-Y. Chen, C.-H. Lin, H.-M. Hsiao *et al.*, "A 28nm 1mb time-domain computing-in-memory 6t-sram macro with a 6.6 ns latency, 1241gops and 37.01 tops/w for 8b-mac operations for edge-ai devices," in *2022 IEEE International Solid-State Circuits Conference (ISSCC)*, vol. 65. IEEE, 2022, pp. 1–3.
- [7] N. Verma, H. Jia, H. Valavi, Y. Tang, M. Ozatay, L.-Y. Chen, B. Zhang, and P. Deaville, "In-memory computing: Advances and prospects," *IEEE Solid-State Circuits Magazine*, vol. 11, no. 3, pp. 43–55, 2019.
- [8] M. Horowitz, "1.1 computing's energy problem (and what we can do about it)," in *2014 IEEE international solid-state circuits conference digest of technical papers (ISSCC)*. IEEE, 2014, pp. 10–14.
- [9] R. Dorrance, D. Dasalukunte, H. Wang, R. Liu, and B. R. Carlton, "An energy-efficient bayesian neural network accelerator with cim and a time-interleaved hadamard digital grng using 22-nm finfet," *IEEE Journal of Solid-State Circuits*, vol. 58, no. 10, pp. 2826–2838, 2023.
- [10] P. Shukla, A. Muralidhar, N. Iliiev, T. Tulabandhula, S. B. Fuller, and A. R. Trivedi, "Ultralow-power localization of insect-scale drones: Interplay of probabilistic filtering and compute-in-memory," *IEEE transactions on very large scale integration (VLSI) systems*, vol. 30, no. 1, pp. 68–80, 2021.
- [11] R. Cai, A. Ren, N. Liu, C. Ding, L. Wang, X. Qian, M. Pedram, and Y. Wang, "Vibnn: Hardware acceleration of bayesian neural networks," *ACM SIGPLAN Notices*, vol. 53, no. 2, pp. 476–488, 2018.
- [12] J. Xu, Y. Shen, E. Chen, and V. Chen, "Bayesian neural networks for identification and classification of radio frequency transmitters using power amplifiers' nonlinearity signatures," *IEEE Open Journal of Circuits and Systems*, vol. 2, pp. 457–471, 2021.
- [13] H. Fan, M. Ferianc, Z. Que, S. Liu, X. Niu, M. R. Rodrigues, and W. Luk, "Fpga-based acceleration for bayesian convolutional neural networks," *IEEE Transactions on Computer-Aided Design of Integrated Circuits and Systems*, vol. 41, no. 12, pp. 5343–5356, 2022.
- [14] D.-U. Lee, W. Luk, J. D. Villasenor, G. Zhang, and P. H. W. Leong, "A hardware gaussian noise generator using the wallace method," *IEEE Transactions on Very Large Scale Integration (VLSI) Systems*, vol. 13, no. 8, pp. 911–920, 2005.
- [15] D. B. Thomas and W. Luk, "Multiplierless algorithm for multivariate gaussian random number generation in fpgas," *IEEE transactions on very large scale integration (VLSI) systems*, vol. 21, no. 12, pp. 2193–2205, 2013.
- [16] H. Fan, M. Ferianc, Z. Que, X. Niu, M. Rodrigues, and W. Luk, "Accelerating bayesian neural networks via algorithmic and hardware optimizations," *IEEE Transactions on Parallel and Distributed Systems*, vol. 33, no. 12, pp. 3387–3399, 2022.
- [17] E. Goan and C. Fookes, "Bayesian neural networks: An introduction and survey," *Case Studies in Applied Bayesian Data Science: CIRM Jean-Morlet Chair, Fall 2018*, pp. 45–87, 2020.
- [18] S. Yu, H. Jiang, S. Huang, X. Peng, and A. Lu, "Compute-in-memory chips for deep learning: Recent trends and prospects," *IEEE circuits and systems magazine*, vol. 21, no. 3, pp. 31–56, 2021.
- [19] X. Zhang, A. Huang, Q. Hu, Z. Xiao, and P. K. Chu, "Neuromorphic computing with memristor crossbar," *physica status solidi (a)*, vol. 215, no. 13, p. 1700875, 2018.
- [20] C.-J. Jhang, C.-X. Xue, J.-M. Hung, F.-C. Chang, and M.-F. Chang, "Challenges and trends of sram-based computing-in-memory for ai edge devices," *IEEE Transactions on Circuits and Systems I: Regular Papers*, vol. 68, no. 5, pp. 1773–1786, 2021.
- [21] C. Li, Z. Wang, M. Rao, D. Belkin, W. Song, H. Jiang, P. Yan, Y. Li, P. Lin, M. Hu *et al.*, "Long short-term memory networks in memristor crossbar arrays," *Nature Machine Intelligence*, vol. 1, no. 1, pp. 49–57, 2019.
- [22] S. Jung, H. Lee, S. Myung, H. Kim, S. K. Yoon, S.-W. Kwon, Y. Ju, M. Kim, W. Yi, S. Han *et al.*, "A crossbar array of magnetoresistive memory devices for in-memory computing," *Nature*, vol. 601, no. 7892, pp. 211–216, 2022.
- [23] D. Bonnet, T. Hirtzlin, A. Majumdar, T. Dalgaty, E. Esmanhotto, V. Meli, N. Castellani, S. Martin, J.-F. Nodin, G. Bourgeois *et al.*, "Bringing uncertainty quantification to the extreme-edge with memristor-based bayesian neural networks," *Nature Communications*, vol. 14, no. 1, p. 7530, 2023.
- [24] M. S. Turan, E. Barker, J. Kelsey, K. A. McKay, M. L. Baish, M. Boyle *et al.*, "Recommendation for the entropy sources used for random bit generation," *NIST Special Publication*, vol. 800, no. 90B, p. 102, 2018.
- [25] B. Sunar, "True random number generators for cryptography," *Cryptographic Engineering*, pp. 55–73, 2009.
- [26] S. Taneja, V. K. Rajanna, and M. Alioto, "In-memory unified trng and multi-bit puf for ubiquitous hardware security," *IEEE Journal of Solid-State Circuits*, vol. 57, no. 1, pp. 153–166, 2021.
- [27] V. Tripathi and B. Murmann, "Mismatch characterization of small metal fringe capacitors," *IEEE Transactions on Circuits and Systems I: Regular Papers*, vol. 61, no. 8, pp. 2236–2242, 2014.
- [28] B. Cheng, J. Liu, S. Davis, Z. M. Enciso, L. Pei, M. Chang, and N. Cao, "A 65nm neuromorphic bio-signal encoder with compute-in-entropy architecture 7.13 nj privacy-preserving encoding and 2.38 mb/mm² item memory density," in *2024 IEEE Symposium on VLSI Technology and Circuits (VLSI Technology and Circuits)*. IEEE, 2024, pp. 1–2.
- [29] N. Dalal and B. Triggs, "Histograms of oriented gradients for human detection," in *2005 IEEE computer society conference on computer vision and pattern recognition (CVPR'05)*, vol. 1. Ieee, 2005, pp. 886–893.
- [30] A. G. Howard, M. Zhu, B. Chen, D. Kalenichenko, W. Wang, T. Weyand, M. Andreetto, and H. Adam, "Mobilenets: Efficient convolutional neural networks for mobile vision applications," 2017. [Online]. Available: <https://arxiv.org/abs/1704.04861>
- [31] C. Guo, G. Pleiss, Y. Sun, and K. Q. Weinberger, "On calibration of modern neural networks," in *International conference on machine learning*. PMLR, 2017, pp. 1321–1330.